A Parametric Model for Studying the Aorta Hemodynamics by means of the Computational Fluid Dynamics

M. Cilla[a,b,c], M. Casales[b], E. Peña[b,c], M. A. Martínez[b,c], M. Malvè[b,c,d,*]

[a] *Centro Universitario de la Defensa (CUD), Academia General Militar, Ctra. de Huesca s/n, E-50090 Zaragoza, Spain*

[b] *Aragón Institute of Engineering Research (I3A). Universidad de Zaragoza, C/María de Luna s/n, E-50018, Zaragoza, Spain*

[c] *Centro de Investigación Biomédica en Red en Bioingeniería Biomateriales y Nanomedicina (CIBER-BBN), C/Poeta Mariano Esquillor s/n, E-50018, Zaragoza, Spain*

[d] *Public University of Navarre, Department of Engineering, Edif. de los Pinos, Campus Arrosadía s/n, E-31006, Pamplona, Spain*

Abstract

Perturbed aorta hemodynamics, as for the carotid and the coronary artery, has been identified as potential predicting factor for cardiovascular diseases. In this study, we propose a **parametric study** based on the computational fluid dynamics with the aim of providing information regarding aortic disease. In particular, the blood flow inside a parametrized aortic arch is computed as a function of morphological changes of baseline aorta geometry. Flow patterns, wall shear stress, time average wall shear stress and oscillatory shear index were calculated during the cardiac cycle. The influence of geometrical changes on the hemodynamics and on these variables was evaluated. **The results suggest that the distance between inflow and aortic arch and the angle between aortic arch and descending trunk are the most influencing parameters regarding the WSS-related indices while the effect of the inlet diameter seems limited. In particular, an increase of the aforementioned distance produces a reduction of the spatial distribution of the higher values of the time average wall shear stress and of the oscillatory shear index independently on the other two parameters while an increase of the angle produce an opposite effect. Moreover, as expected, the analysis of the wall shear stress descriptors suggests that the inlet diameter influences only the flow intensity.** As conclusion, the proposed **parametric study** can be used to evaluate the aorta hemodynamics and could be also applied in the future, for analyzing pathological cases and virtual situations, such as pre- and/or post-operative cardiovascular surgical states that present enhanced changes in the aorta morphology yet promoting important variations on the considered indexes.

Key words: Aortic hemodynamics, Wall shear stress descriptors, Finite Volume Analysis, Parametric aorta design, Computational Fluid Dynamics.

---

1 Introduction

There are many evidences that correlate cardiovascular diseases with highly disturbed flow in human aorta, predominantly in locations near the aortic arch branches, and the bend of the

* Corresponding author.
Email address: mauro.malve@unavarra.es (M. Malvè).

descending trunk. In the literature it is stated that these locations, due to the inherent geometrical features, show oscillatory wall shear stress (WSS), which might promotes vascular diseases (DeBakey et al., 1985; Ku et al., 1985; Chiu et al., 2009; Lantz et al., 2012; Numata et al., 2016). The mentioned geometrical features include tapering, high curvature ratio and angled branching. In addition, the aortic flow is caused by the ventricular contraction that generates a very complex inflow through the aortic valve. The prediction of aortic diseases are mainly based on symptoms or geometrical and morphological factors evidenced during specific examinations, such as the size of the aorta (Erbel et al., 2014; Numata et al., 2016). However, other indicators are needed for improving the diagnosis. In this context, the hemodynamic parameters, such as blood flow velocity, blood pressure and especially WSS, play a very important role in the pathophysiology of aortic diseases (Numata et al., 2016). It is well established that WSS-related indexes are potential indicators for atherosclerosis risk (Caro et al., 1971; Ku et al., 1985; Malek et al., 1999). The latter is usually obtained through the computational fluid dynamics (CFD) that could be useful as non invasive predicting tool in the clinical practice. The CFD, especially when coupled with image-based models, allows for a detailed description of the hemodynamics in human vessels, providing spatial and temporal distribution of flow, pressure and WSS. In the past years, a considerable number of works have tried to address the aortic flow, attempting to resolve the intricated fluid structures (Liu et al., 2011) yet providing the challenging quantification of flow disturbed indicators (Morbiducci et al., 2011; Gallo et al., 2012; Caballero and Laín, 2013; Morbiducci et al., 2013), the endothelial shear stress and its related indices (Lantz et al., 2011, 2012; Numata et al., 2016). High performance numerical models have been proposed for solving the tridimensional flow including turbulence modelling (Lantz et al., 2011, 2012; Wendell et al., 2013; Binter et al., 2016) and experimental works that help improving the accuracy of computational simulations (Gülan et al., 2012; Hope et al., 2013; Kousera et al., 2013; Gülan et al., 2017; Callaghan and Grieve, 2017; Menut et al., 2018). The influence of the boundary conditions, that from decades is debated among the scientific community, has been also accurately analyzed in (Kim et al., 2009; Spilker and Taylor, 2010; Morbiducci et al., 2013; Pirola et al., 2017) among others. With the aim of providing details of the aortic blood flow and the derived wall shear stress and related variables as a function of different aorta morphologies, we propose a parametrized model. The latter is based on three main parameters, i.e. the aortic inlet diameter, the aortic arch width and the angle between the aortic arch and the descending trunk. The hemodynamic consequences of the variation of these parameters are evaluated by means of a qualitative and quantitative analysis of the blood flow structures and the WSS-related variables such as the time average wall shear stress (TAWSS) and the oscillatory shear index (OSI) along the aorta model. **The advantage of the proposed parametric study is that it could be used for studying the aorta hemodynamics in variable conditions such as pathological and/or virtual situations**. As an example it could be useful for the prediction of pre- and/or post-operative cardiovascular surgical states that present enhanced morphological variations on the hemodynamics indexes.

2 Materials and methods

2.1 Parametric aorta model

The idealized parametric model of human aorta was built to carry out a comprehensive CFD parametric study for investigating the influence of the essential geometrical factors related to aorta hemodynamics. The main geometry created using mean dimensions was parametrized through the commercial software SolidWorks (Dessault Systèmes, Vélizy-Villacoublay, France). The latter was linked with the commercial package Ansys Workbench (Ansys Inc., Canonsburg, PE, USA). In this framework, the computational grids (with Ansys IcemCFD), the numerical models (with Ansys CFX), the simulations (with Ansys CFX) and the post-processing of the results (with Ansys CFD Post) were carried out. **The used commercial software can be linked using the utilities options of Ansys and the add-in tool of SolidWorks. In this way, a variation of a single parameter on the geometry of a specific model is immediately updated on the numerical model. Finally, the latter need only to be computed and post processed. This process has been followed for all the 27 performed computations. The main dimensions of the aorta morphology considered in this work were obtained starting from a data set of 5 patient specific human aortas. Subjects undergoing standard-of-care contrast enhanced computed tomography (CT) to rule out potential coronary artery disease were considered for this study. In particular, a total of 5 adult subjects with no radiological findings were retrospectively included. Each set of images was treated by means of the Brilliance Workspace Portal (Koninklijke Philips N.V., High, Eindhoven, The Netherlands). In this software, a three dimensional model was created and exported as STL (Stereo Lithography) file. The images are shown in the Figure 1. In SolidWorks, the main dimensions of the patient-specific aorta geometries were measured. In the Table 1, the main dimensions of the 5 patient specific aorta are shown. The latter includes the inlet and outlet diameter of the aorta, as well as the diameters of the three main branches of the aortic arch. The tridimensional parametric geome-**

try that results from the 5 patients includes the main physiological characteristics of the aortic arch represented in the Figure 2A. The range of the considered parameters was selected considering the geometrical features and variations of these medical images. However, even 5 subjects is a small population, the values assigned to the parameters are in physiological range respect to other literature data (Morbiducci et al., 2011; Frydrychowicz et al., 2012; Gallo et al., 2012; Nordmeyer et al., 2013). The aortic arch geometry incorporates their three main branches, that is, the brachiocephalic trunk or anonymous artery, the carotid artery and the subclavian artery. For sake of simplicity, the aortic bulb was neglected (Morbiducci et al., 2011; Gallo et al., 2012; Morbiducci et al., 2013). **For this reason, in all the CT-based geometries, the inlet diameter was not measured at the aortic valve plane but upstream right after the bulb.** As Figure 2A shows, the study includes the variation of three geometrical parameters, which are: The inlet diameter of the aorta (Φ), whose considered values were 18 mm, 22 mm and 26 mm, the angulation of the aortic arch (α), whose studied values were $10°$, $20°$ and $30°$, and the width of the arch of the aorta, which is measured as the linear distance from the aorta inlet to the end of the curvature (d) and whose analyzed values were 72 mm, 75 mm and 78 mm. **The other dimensions to create the baseline geometry were the diameter and the length of the three upper branches of** 6 mm **and** 12 mm**, respectively, the aorta outlet diameter** (20 mm) **and the total height of the aorta** (176 mm). Therefore, three geometrical parameters and three values for each were considered and combined for a total of 27 computational models **as summarized in the Table 2 and in the Figure 3.**

2.2 Numerical discretization

The computational meshes were created using the commercial software Ansys Icem-CFD v. 16.0 (ANSYS Inc. Canonsburg, Pennsylvania, USA). The used tetrahedral grid was composed by over $2 \cdot 10^6$ tetrahedral cells. The latter includes a 5-prism layer for capturing the turbulent boundary layer at the aortic walls. Additionally, considering the $k-\omega$-SST turbulent model used for the computation, a dimensionless wall distance less than 1 was used ($y^+ < 1$).

Prior to the computations, a mesh independence study was carried out. Coarser and finer meshes of about 0.5×10^6, 1×10^6, 2×10^6, 4×10^6 and 8×10^6 elements respectively were tested and the selected grid provided an error on the velocity profile of less than 3% with respect to finer meshes. On the contrary, the error of the

Table 1
Dimensions (in $[mm]$) of the diameters of the main branches of the five patient-specific aorta geometries used as basis for the parameters of the computed models.

	Aorta inlet	Aorta outlet	Anonima outlet	Carotid outlet	Subclavian outlet
Patient #1	21.521	16.4	13.9	7.758	6.2945
Patient #2	24.835	23.54	8.577	8.8025	6.7935
Patient #3	22.233	22.39	11.675	10.9885	6.3565
Patient #4	25.208	16.85	11.4625	7.3645	6.884
Patient #5	19.038	14.06	9.993	2.7865	6.272

Table 2
Parameters and corresponding values of the parametric model.

Parameter			
α [°]	10	20	30
Φ $[mm]$	18	22	26
d $[mm]$	72	75	78

computed WSS values within different meshed was less than 5%. The independence study shows different errors depending on the variable. According to Prakash et al. (Prakash and Ethier, 2001), achieving mesh independence in computed WSS fields requires an extremely large number of nodes. The grid chosen for the computation guarantees from one side adequate convergence of the velocity and WSS and, in the other side, reasonable computational costs taking into consideration the limitations on the software capability as well as its degree of accuracy (Prakash and Ethier, 2001).

Different element sizes were used for the spatial discretization, according to the complexity of the different areas of the model, as depicted in the Figure 2B. A general element size of $5 \times 10^{-4}\ mm$ was used for meshing the computational volume. However, the anonymous, carotid and subclavian arteries and their intersection with the aorta as well as the inlet and outlet of the aorta were meshed with a size of $2 \times 10^{-4}\ mm$.

2.3 Material properties

The blood flow was modeled as turbulent, incompressible (density, $\rho = 1050\ \frac{Kg}{m^3}$) and non-Newtonian, using the Carreau constitutive law. The Carreau model assumes that the viscosity of blood, μ, varies according to the following equation:

$$\mu = \mu_\infty + (\mu_0 - \mu_\infty) \cdot (1 + A_c \dot{\gamma}_{ij}^2)^{m_c} \tag{1}$$

where μ_0 and μ_∞ are low and high shear rate asymptotic values, while the parameters A_c and m control the transition region size. The Carreau blood model predicts decreasing viscosity at high strain. For this study we used the experimental values provided in (Valencia and Baeza, 2009): $\mu_0 = 0.056 \ \frac{N \cdot s}{m^2}$, $\mu_\infty = 0.00345 \ \frac{N \cdot s}{m^2}$ $A_c = 10.975$ and $m_c = -0.3216$.

2.4 Hemodynamics indexes

We evaluated the following wall shear stress (WSS)-related variables: time average wall shear stress (TAWSS) and the oscillatory index (OSI). These variables were computed starting from the instantaneous WSS vector $\vec{\tau_w}$ **and saved** at each time instant of the cardiac cycle T. The TAWSS for pulsatile flow, represents the spatial distribution of the tangential, frictional stress caused by the action of blood flow on the vessel wall temporally averaged on the entire cardiac cycle:

$$TAWSS = \frac{1}{T} \int_0^T |\vec{\tau_w}| dt \tag{2}$$

The OSI is a non-dimensional parameter that measures the directional change of WSS during the cardiac cycle (He and Ku, 1996) and it is adopted for describing the disturbance of a flow field:

$$OSI = 0.5 \left(1 - \frac{| \int_0^T \vec{\tau_w} dt |}{\int_0^T |\vec{\tau_w}| dt} \right) \tag{3}$$

2.5 Boundary conditions

The computational model was considered as rigid and a no slip condition was applied to the external vessel walls. **Aortic blood flow was imposed at the inlet and at the outlets of each model**. A physiological aortic flow waveform, which was extracted from Kousera et al. (Kousera et al., 2012), was applied at the inlet of each model. For the boundary conditions of the upper outlets (anonymous, carotid and subclavian arteries) and the lower outlet (aortic trunk outlet), the Murray's law (Murray, 1926) was used. The blood flow entering the aorta was systematically divided through the outlets considering that the cube of the radius (r) of a blood vessel is equal to the sum of the cubes of the radii of its n branches (r_1, r_2 ... r_n),

$$r^3 = {r_1}^3 + {r_2}^3 + ... + {r_n}^3.$$

This law also states that there is a functional relationship between the radius of the vessel and the volumetric flow that passes through it. Accordingly to this law, the same relationship is valid for the velocity profile, the tangential tension of the wall, the Reynolds number or the pressure gradient, among others. **The Murray's law proposes a cubic relation of the radius with the volumetric flow (Q), that is, $Q \propto r^3$. However, further studies have proposed a new generic interrelation, such as $Q \propto r^c$, where c is a parameter determined from the minimum energy condition (Revellin et al., 2009). This value usually ranges between 2 and 3 within the arterial system (Olufsen et al., 2000). In particular, it is stated that the exponent c takes a value of 2 in the largest blood vessels as the aorta and a value of 3 in small arteries such as arterioles and capillaries**. For this reason, in this work, the flow of the aorta outlet and the three branches was defined as dependent on the square of the radius of the blood vessel (i. e. $c = 2$).

2.6 Numerical modelling

The numerical simulations were performed in Ansys CFX v. 16.0 (ANSYS Inc. Canonsburg, Pennsylvania, USA). A sensitivity analysis showed that a time step size of 0.001 s was necessary for correctly resolving the flow features. We used a convergence criteria of 10^{-5}. Both spatial and temporal discretization schemes were second-order accurate. For dumping the effects of the initial transient, three cardiac cycles were simulated and the results obtained from the last cycle were evaluated. Data were saved every 0.01 s during the last cardiac cycle. **For the present analysis the aortic blood flow was considered as turbulent. In particular, the $k - \omega$ - SST model was considered (Gallo et al., 2012; Morbiducci et al., 2013). Medium turbulence intensity (ratio of the root-mean-square of the velocity fluctuations, u', to the mean flow velocity, u_{avg}) has been selected at the inflow boundary conditions that correspond to 5%.**

In order to dump the influence of the boundary conditions imposition, 5-diameter long inlet, outlet and branches extensions were added to the models. Plugged velocity profiles were applied to the inlet and outlets extensions which lengths provided fully developed flow on the computational region of interest. Finally, considering the inlet sections (18, 22 and 26 mm) and the peak velocity flow (0.97 m/s), the computed Reynolds number was of 5196.4, 6351.2 and 7506 respectively.

3 Results

3.1 Flow patterns

Hemodynamic outcomes resulting from the computational study (Figure 4), are visualized using streamlines, which are colored using the velocity magnitude. In this Figure, the flow is represented as hemodynamic snapshot at peak systole. From the Figure 4, as expected, it is visible that at the aorta entrance, the blood flow velocity is higher for the models with $\Phi = 18\ mm$, ($v \approx 2\ m/s$) independently on the values of the angle α. Of course, an increase of the inlet diameter provokes as a consequence a reduction of the intensity of the velocity. However, the Figure 4 shows that also the variation of the angle α impacts the blood flow structures. An increase of this variable, independently on the inlet diameter Φ, suggests an increase of the local acceleration that appears at the inferior wall of the aortic arch. Furthermore, the angle of the aortic arch causes a slight reduction of the blood flow intensity ($v \approx 0.5\ m/s$) on the superior descending aorta that is basically visible in all the presented models and seems to be not dependent on any model variations. Also, the arch curvature promotes a secondary flow that can be found in all the computed models and it is independent on the parametric variations.

As widely known, the WSS depends on the velocity and on the aortic geometries. Lower regions of the WSS ($\approx 2\ Pa$) are located at the beginning of the descending trunk and at the inferior wall of the aortic arch for all models (results not shown), independently on the parametric variations. In these locations, as found by other authors (Liu et al., 2011; Gallo et al., 2012; Morbiducci et al., 2013), the blood flow tends in fact to recirculate. Generally speaking, the WSS tends to reduce for increasing inlet diameter Φ and arch width d. **The blood flow evidences a moderated recirculation in the models with $\Phi = 30^\circ$ so that the WSS values, and, as a consequence the TAWSS, tend to increase with respect to the models with $\Phi = 10^\circ$ and $\Phi = 20^\circ$.**

3.2 Time Average Wall Shear Stress and Oscillatory Shear Index

The recirculation due to the aortic arch curvature and the secondary flow that develops in the aortic trunk promote a region in the anterior wall of the descending trunk characterized by low and oscillatory wall shear stress. This is visualized by means of the spatial distribution of the TAWSS and the OSI in the Figures 5 and 6 respectively. The TAWSS, being an averaged variable, tends to smooth the differences of the spatial distribution that can enhance the WSS. In general, the lowest values of the TAWSS are located at the inferior aortic arch wall and at the external side of the descending trunk. In particular, at this location, two different regions are depicted: at the beginning and slightly downstream. As aforementioned, these two regions are promoted by the flow recirculation and by the secondary flow that originate because of the high curvature of the aortic arch. Local recirculation have been also found at the intersection of the aortic arch with the superior branches. **Independently on the parameters α and Φ, the spatial distribution of the high TAWSS ($> 20\ Pa$) is particularly extended at the arch for $d = 72\ mm$. An increase of d promotes a reduction of this distribution, as visible also in the Figure 7 by means of histograms plotted as a function of the normalized area. A clearer picture in this sense is given by the spatial distribution of the OSI. There**

is a marked location of the high value for this variable. This is located on the descending trunk. It is visible a relative insensitivity of the OSI spatial distribution with the inlow diameter Φ. On the contrary, the parameters that most impacts in this sense seems to be the angle α and especially the distance d, accordingly with the findings of the distribution of TAWSS. From the performed simulations, it is suggested that an increase of this angle causes and increase of the region affected by high OSI at the aortic arch and a contemporary decrease of the region affected by high OSI at the descending trunk. While the regions characterized by elevated OSI extend, their values tend to be constant $(0.45 \approx 0.5)$. Contrary to this, an increase of d promotes a decrease of the distributions of the high OSI values. These two findings are visible also in the Figure 8.

From both Figures 7 and 8 it seems that the change of the parameters d and α influences the percentage of aortic area characterized by high TAWSS and OSI. On the contrary, the diameter Φ of the aorta inlet seems to influence only slightly the distribution of TAWSS and OSI, as the main effect of an increase of this parameter suggests a decrease of the velocity. The TAWSS tends to slightly reduce for increasing Φ as it is expected.

From the histograms it is visible that the highest values of the TAWSS $(\approx 10{-}50\ Pa)$ are located on about the 30% of the aortic surface. Lower values of $(\approx 2-4\ Pa)$ also markedly affect the aorta with similar area percentages $(\approx 40\%)$. On the contrary, lower TAWSS values $(0-2\ Pa)$ which are considered as typical atheroprone WSS phenotype seems to depend mainly on the diameter Φ as the percentage of normalized area are constant for different values of α and d. This tendency is the same for the interval $2-4$ Pa but changes for higher TAWSS values (see Fig. 7). The OSI histograms show, that high values ($\approx 0.4-0.5$) are concentrated on about the 5% of the aortic surface, while a considerable percentage of the aortic walls ($\approx 60\%-70\%$) shows values between 0 and 0.05. The latter can be found at the inferior wall of the aortic arch and descending trunk (see Fig. 6). On the contrary, regions characterized by OSI equals to $\approx 0.4-0.5$ can be mainly found at the descending trunk where the blood flow recirculate a cause of the change in curvature.

4 Discussion

A parametric model of the human aorta was developed with the aim of studying the effect of the aortic morphological changes on the overall hemodynamics. The model is based on three parameters: the aortic inlet diameter Φ, the aortic arch width d and the angle α between the aortic arch and the descending trunk. The TAWSS and the OSI of each variation were studied for evaluating the predisposition of a given morphology to promote a certain endothelial shear distribution. This work may help finding which parameter is more affecting the extension and the intensity of the WSS-indices. Despite the extensive study on the aorta hemodynamics in fact, relevant thresholds and margins that play a role in the prediction of aortic diseases are still lacking. Disturbed flow patterns were observed in healthy subjects by other authors (Morbiducci et al., 2011; Frydrychowicz et al., 2012;

Gallo et al., 2012; Nordmeyer et al., 2013). Respect to these works, the parametric variations, the overall dimensions considered in this study and the findings relative to the WSS-indices are in the same range. The main locations of high TAWSS and especially those of the OSI, (descending trunk and intersection with the brachial, subclavian and carotid arteries) agree well with those found in the literature (Benim et al., 2011; Morbiducci et al., 2011; Gallo et al., 2012; Nordmeyer et al., 2013). On the contrary, some discrepancies affect the computed values, as the parametric models have more smoothed geometrical features respect to the patient specific models used in other studies (Lantz et al., 2011; Crosetto et al., 2011; Raymond et al., 2011).

The presented results show that the geometrical changes promote moderate variations in the hemodynamic solutions. However, important changes can be highlighted. An increase of the inlet diameter promotes a reduction of the WSS related indices in all analyzed models while an increase of the angle between aortic arch and descending aorta suggests an increase of the spatial distribution of the TAWSS and a reduction of the spatial distribution of the OSI in the descending trunk. The width of the aortic arch (parameter d) promotes an increase of lower values of OSI and a reduction of its higher values. However, its amplitude impacts only slightly the flow patterns and consequently the spatial distribution of the TAWSS and of the OSI. Its influence can be observed correctly only considering as well the angle between arch and descending trunk. In particular, the combined increase of both parameters promotes the extensions of the high OSI regions in the internal surface of the aortic arch at the beginning of the trunk.

The WSS gives a measure of the interaction between blood and artery and correlates with exchange processes such as load acting on the endothelial cells (Bruening et al., 2018). However, the predisposition to high or low WSS-related indices and its relationship with the aortic morphology is still debated and other indices as the helicity has been introduced and discussed (Morbiducci et al., 2009, 2011, 2015). However, a parametric study that intends systematically assess the role of different geometric factors on the aorta hemodynamics has been not accomplished yet. From this analysis, it seems that the distance d and the angle α are the most influencing parameters regarding the WSS-related factors while the effect of the inlet diameter Φ is more limited. Previous works have highlighted the role of the aortic arch as the main factor impacting the OSI (Lantz et al., 2011; Liu et al., 2011; Numata et al., 2016). Recent studies analyze the aortic geometry using machine learning (Liang et al., 2011) providing a correlation between geometries and flow and pressure without giving a threshold for WSS indices. Finally, the force distribution has been studies as a function of the aortic tortuosity (Belvroy et al., 2020) with the aim of estimate how an increase of this parameter may affect the hemodynamic displacement forces. A previous study stated that the increase of the arch angulation results in a higher displacement force in this region (Figueroa et al., 2009). Unfortunately, no hemodynamics variables are provided for the aorta as a function of the tortuosity and other geometrical characteristics as performed for coronaries for instance (Xie et al., 2013; Malvè et al., 2015; Liu et al., 2015; Buradi and Mahalingam, 2020). Nevertheless, as the coronary artery, the geometry of the aorta varies from subject to subject so that we believe that this study may be the first

attempt to correlate in a similar way the geometry and the hemodynamics of the aorta.

Several limitations affect the main findings of this study. These have been made to facilitate the study feasibility. In particular, the assumption taken for the valve modeling i.e. the inlet boundary conditions, may impact the presented WSS indices has demonstrated by Morbiducci and coworkers (Morbiducci et al., 2013). Also the absence of a realistic inlet velocity profile considerably affects the main findings. In this work, the flow is applied at the inlet and outlets as flat profile. With adequate extensions, the flow can fully develop at the entrance of the aorta and the effect of the outflow conditions can also be reduced. However, the aortic flow after the valve opening is surely very complicated and not fully developed so that this assumption impacts the blood flow and the WSS in the regions near the aortic arch but also at the aortic trunk. In addition, even the advantage of a parametric studies is that a large number of cases can be analyzed, general conclusions on the WSS and related indices in aorta should be definitively confirmed on a patient-specific dataset.

5 Conclusion

In this paper, we presented **a parametric study for systematically evaluating by means of the computational fluid dynamics the flow patterns and WSS-based indices in the human aorta. The findings of this work show that the models are capable of investigating the role of the aorta morphology in determining the hemodynamics**

variables. The study presents 27 cases with the aim of analyzing the influence of the aorta geometrical parameters on the hemodynamics. In particular, the inlet diameter, the angulation and the width of the aortic arch are considered as parameters. The results show that the distance d and the angle α are the most influencing parameters regarding the WSS-related indices while the effect of the inlet diameter Φ is limited. In particular, an increase of d produces a reduction of the higher values of the TAWSS and OSI spatial distributions independently on the other two parameters while an increase of the angle α produce an opposite effect. Additionally, as expected, the analysis of the WSS indices suggests that the inlet diameter influences only the flow intensity.

Conflict of interest

None of the authors has any financial or personal relationships that could inappropriately influence (bias) their work.

Ethical approval

Not required.

Acknowledgments

The authors gratefully acknowledge the research support of the Spanish Ministry of Economy and Competitiveness through the research projects DPI-2016-76630-C2-1-R and DPI2017-83259-R (AEI/FEDER,UE). The support of the Instituto de Salud Carlos III (ISCIII) through the CIBER-BBN initiative and the project Patient-Specific Modelling of the Aortic valve replacement: Advance towards a Decision Support System (DeSSAValve) is highly appreciated.

References

Belvroy, V. M., Romarowski, R. M., Theodorus, van Bakel, M. J., van Herwaarden, J. A., Bismuth, J., Auricchio, F., Moll, F. L., Trimarchi, S., 2020. Impact of aortic tortuosity on displacement forces in descending thoracic aortic aneurysms. European Journal of Vascular and Endovascular Surgery, In Press.

Benim, A. C., Nahavandi, A., Assmann, A., Schubert, D., Feindt, P., Suh, S. H., 2011. Simulation of blood flow in human aorta with emphasis on outlet boundary conditions. Applied Mathematical Modelling 35 (7), 3175–3188.

Binter, C., Gülan, U., Holzner, M., Kozerke, S., 2016. On the accuracy of viscous and turbulent loss quantification in stenotic aortic flow using phase-contrast MRI. Magnetic Resonance in Medicine 76, 191–196.

Bruening, J., Hellmeier, F., Yevtushenko, P., Kelm, M., Nordmeyer, S., Sündermann, S. H., Kuehne, T., Goubergrits, L., 2018. Impact of patient-specific LVOT inflow profiles on aortic valve prosthesis and ascending aorta hemodynamics. Journal of Computational Science 24, 91–100.

Buradi, A., Mahalingam, A., 2020. Impact of coronary tortuosity on the artery hemodynamics. Biocybernetics and Biomedical Engineering 40 (1), 126–147.

Caballero, A. D., Laín, S., 2013. A review on computational fluid dynamics modelling in human thoracic aorta. Cardiovascular Engineering Technology 4 (2), 103–130.

Callaghan, F. M., Grieve, S. M., 2017. Spatial resolution and velocity field improvement of 4D-flow MRI. Magnetic Resonance in Medicine 78, 1959–1968.

Caro, C. G., Fitz-Gerald, J. M., Schroter, R. C., 1971. Atheroma and arterial wall shear. Observation and proposal of a shear dependent mass transfer mechanism for atherogenesis. Proceedings of the Royal Society B: Biological Sciences 177 (1046), 109–159.

Chiu, J. J., Usami, S., Chien, S., 2009. Vascular endothelial responses to altered shear stress: pathologic implications for atherosclerosis. Annals of Medicine 41, 19–28.

Crosetto, P., Raymond, P., Deparis, S., Kontaxakis, D., Stergiopulos, N., Quarteroni, A., 2011. Fluid-structure interaction simulation of aortic blood flow. Computers and Fluids 43 (1), 46–57.

DeBakey, M. E., Lawrie, G. M., Glaeser, D. H., 1985. Patterns of atherosclerosis and their surgical significance. Annals of Surgery 20 (2), 115–131.

Erbel, R., Aboyans, V., Boileau, C., Bossone, E., Di Bartolomeo, R., Eggebrecht, H., Evangelista, A., Falk, V., Frank, H., Gaemperli, O., Grabenwöger, M., Haverich, A., Iung, B., Manolis, A. J., Meijboom, F., Nienaber, C. A., Roffi, M., Rousseau, H., Sechtem, U., Sirnes, P. A., Allmen, R. S., Vrints, C. J., 2014. Esc guidelines on the diagnosis and treatment of aortic diseases. European Heart Journal 35, 2873–2896.

Figueroa, C. A., Taylor, C. A., Chiou, A. J., Yeh, V., Zarins, C. K., 2009. Magnitude and direction of pulsatile displacement forces acting on thoracic aortic endografts. Journal of Endovascular Therapy 16, 350–358.

Frydrychowicz, A., Berger, A., Muñoz del Rio, A., Russe, M. F., Bock, J., Harloff, A., Markl, M., 2012. Interdependencies of aortic arch secondary flow patterns, geometry, and age analysed by 4-Dimensional phase contrast magnetic resonance imaging at 3 tesla. European Radiology 22, 1120–1130.

Gallo, D., De Santis, G., Negri, F., Tresoldi, D., Ponzini, R., Massai, D., Deriu, M. A., Segers, P., Verhegghe, B., Rizzo, G., Morbiducci, U., 2012. On the use of in vivo measured flow rates as boundary conditions for image-based hemodynamic models of the human aorta: implications for indicators of abnormal flow. Annals of Biomedical Engineering 40 (3), 729–741.

Gülan, U., Binter, C., Kozerke, S., Holzner, M., 2017. Shear-scaling-based approach for irreversible energy loss estimation in stenotic aortic flow - an in vitro study. Journal of Biomechanics 56, 89–96.

Gülan, U., Lüthi, B., Holzner, M., Liberzon, A., Tsinober, A., Kinzelbach, W., 2012. Experimental study of aortic flow in the ascending aorta via particle tracking velocimetry. Experiments in Fluids 53, 1469–1485.

He, X., Ku, D. N., 1996. Pulsatile flow in the human left coronary artery bifurcation: average conditions. Journal of Biomechanical Engineering 118 (1), 74–82.

Hope, M. D., Sedlic, T., Dyverfeldt, P., 2013. Cardiothoracic magnetic resonance flow imaging. Journal of Thoracic Imaging 28 (4), 217–230.

Kim, H. J., Vignon-Clementel, I. E., Figueroa, C. A., LaDisa, J. F., Jansen, K. E., Feinstein, J. A., Taylor, C. A., 2009. On coupling a lumped parameter heart model and a three-dimensional finite element aorta model. Annals of Biomedical Engineering 37, 2153–2169.

Kousera, C. A., Wood, N. B., Seed, W. A., Torii, R., OÕRegan, D., Xu, X. Y., 2012. A numerical study of aortic flow stability and comparison with in vivo flow measurements. Journal of Biomechanics Engineering 135 (1), 011003.

Kousera, C. A., Wood, N. B., Seed, W. A., Torii, R., Regan, D., Xu, X. Y., 2013. A numerical study of aortic flow stability and comparison with in vivo flow measurements. Journal of Biomechanical Engineering 135 (1), 011003.

Ku, D. N., Giddens, D. P., Zarins, C. K., Glagov, S., 1985. Pulsatile flow and atherosclerosis in the human carotid bifurcation. positive correlation between plaque location and low oscillating shear stress. Arteriosclerosis 5, 293–302.

Lantz, J., Gårdhagen, R., Karlsson, M., 2012. Quantifying turbulent wall shear stress in a subject specific human aorta using large eddy simulation. Medical Engineering & Physics 34, 1139–1148.

Lantz, J., Renner, J., Karlsson, M., 2011. Wall shear stress in a subject specific human aorta - influence of fluid-structure interaction. International Journal of Applied Mechanics 3 (4), 759–778.

Liang, L., Mao, W., Sun, W., 2011. A feasibility study of deep learning for predicting hemodynamics of human thoracic aorta. Journal of Biomechanics 99, 109544.

Liu, G., Wu, J., Ghista, D. N., Huang, W., Wong, K. K. L., 2015. Hemodynamic characterization of transient blood flow in right coronary arteries with varying curvature and side-branch bifurcation angles. Computers in Biology and Medicine 64, 117–126.

Liu, X., Fan, Y., Deng, X., Zhan, F., 2011. Effect of non newtonian and pulsatile blood flow on mass transport in the human aorta. Journal of Biomechanics 44, 1123–1131.

Malek, A. M., Alper, S. L., Izumo, S., 1999. Hemodynamic shear stress and its role in atherosclerosis. Journal of the American Medical Association 282 (1), 2035–2042.

Malvè, M., Gharib, A. M., Yazdani, S. K., Finet, G., Martínez, M. A., Pettigrew, R., Ohayon, J., 2015. Tortuosity of coronary bifurcation as a potential local risk factor for atherosclerosis: Cfd steady state study based on in vivo dynamic ct measurements. Annals of Biomedical Engineering 43 (1), 82–93.

Menut, M., Boussel, L., Escriva, X., Bou-Saïd, B., Walter-Le Berre, H., Marchesse, Y., Millon, A., Della Schiava, N., Lermusiaux, P., Tichy, J., 2018. Comparison between a generalized newtonian model and a network-type multiscale model for hemodynamic behavior in the aortic arch: Validation with 4D MRI data for a case study. Journal of Biomechanics 73, 119–126.

Morbiducci, U., Gallo, D., Cristofanelli, S., Ponzini, R., Deriu, M. A., Rizzo, G., Steinman, D. A., 2015. A rational approach to defining principal axes of multidirectional wall shear stress in realistic vascular geometries, with application to the study of the influence of helical flow on wall shear stress directionality in aorta. Journal of Biomechanics 48 (1), 899–906.

Morbiducci, U., Ponzini, R., Gallo, D., Bignardi, C., Rizzo, G., 2013. Inflow boundary conditions for image-based computational hemodynamics: impact of idealized versus measured velocity profiles in the human aorta. Journal of Biomechanics 46 (1), 102–109.

Morbiducci, U., Ponzini, R., Rizzo, G., Cadioli, M., Esposito, A., De Cobelli, F., Del Maschio, A., Montevecchi, F. M., Redaelli, A., 2009. *In Vivo* Quantification of Helical Blood Flow in Human Aorta by Time-Resolved Three-Dimensional Cine Phase Contrast Magnetic Resonance Imaging. Annals of Biomedical Engineering 37 (3), 516–531.

Morbiducci, U., Ponzini, R., Rizzo, G., Cadioli, M., Esposito, A., Montevecchi, F. M., Redaelli, A., 2011. Mechanistic insight into the physiological relevance of helical blood flow in the human aorta. an in vivo study. Biomechanics and Modelling in Mechanobiology 10, 339–355.

Murray, C. D., 1926. The physiological principle of minimum work: I. the vascular system and the cost of blood volume. Proceedings of National Academy of Sciences 12 (3), 207–214.

Nordmeyer, S., Riesenkampff, E., Messroghli, D., S.Kropf, Nordmeyer, J., Berger, F., Kuehne, T., 2013. Four-Dimensional velocity-encoded magnetic resonance imaging improves blood flow quantification in patients with complex accelerated flow. Journal of Magnetic Resonance Imaging 37, 209–221.

Numata, S., Itatani, K., Kanda, K., Doi, K., Yamazaki, S., Morimoto, K., Manabe, K., Ikemoto, K., Yaku, H., 2016. Blood flow analysis of the aortic arch using computational fluid dynamics. European Journal of Cardio-Thoracic Surgery 49, 1578–1585.

Olufsen, M. S., Peskin, C. S., Kim, W. Y., Pedersen, E. M., Nadim, A., Larsen, J., 2000. Numerical Simulation and Experimental Validation of Blood Flow in arteries with Structured-Tree Outflow Conditions. Annals of Biomedical Engineering 28, 1281–1299.

Pirola, S., Cheng, Z., Jarral, O. A., O'Regan, D. P., Pepper, J. R., Athanasiou, T., Xu, X. Y., 2017. On the choice of outlet boundary conditions for patient-specific analysis of aortic flow using computational fluid dynamics. Journal of Biomechanics 60, 15–21.

Prakash, S., Ethier, C. R., 2001. Requirements for mesh resolution in 3D computational hemodynamics. ASME Journal of Biomechanical Engineering 123 (2), 134–144.

Raymond, P., Crosetto, P., Deparis, S., Quarteroni, A., Stergiopulos, N., 2011. Physiological simulation of blood flow in the aorta: Comparison of hemodynamic indices as predicted by 3-D FSI, 3-D rigid wall and 1-D models. Medical Engineering and Physics 35, 784–791.

Revellin, R., Rousset, F., Baud, D., Bonjour, J., 2009. Extension of Murray's law using a non-

Newtonian model of blood flow. Theoretical Biology and Medical Modelling 6 (1), 7.

Spilker, R. L., Taylor, C. A., 2010. Tuning multidomain hemodynamic simulations to match physiological measurements. Annals of Biomedical Engineering 38, 2635–2648.

Valencia, A., Baeza, F., 2009. Numerical simulation of Fluid-Structure Interaction in stenotic arteries considering two layer nonlinear anisotropic structural model. International Communications in Heat and Mass Transfer 36, 137–142.

Wendell, D. C., Samyn, M., Cava, J. R., Ellwein, L. M., Krolikowski, M. M., Gandy, K. L., Pelech, A. N., Shadden, S. C., LaDisa Jr., J. F., 2013. Including aortic valve morphology in computational fluid dynamics simulations: Initial findings and application to aortic coarctation. Medical Engineering and Physics 35, 723–735.

Xie, X., Wang, Y., Zhou, H., 2013. Impact of coronary tortuosity on the coronary blood flow: A 3d computational study. Journal of Biomechanics 46 (11), 1833–1841.

Figures

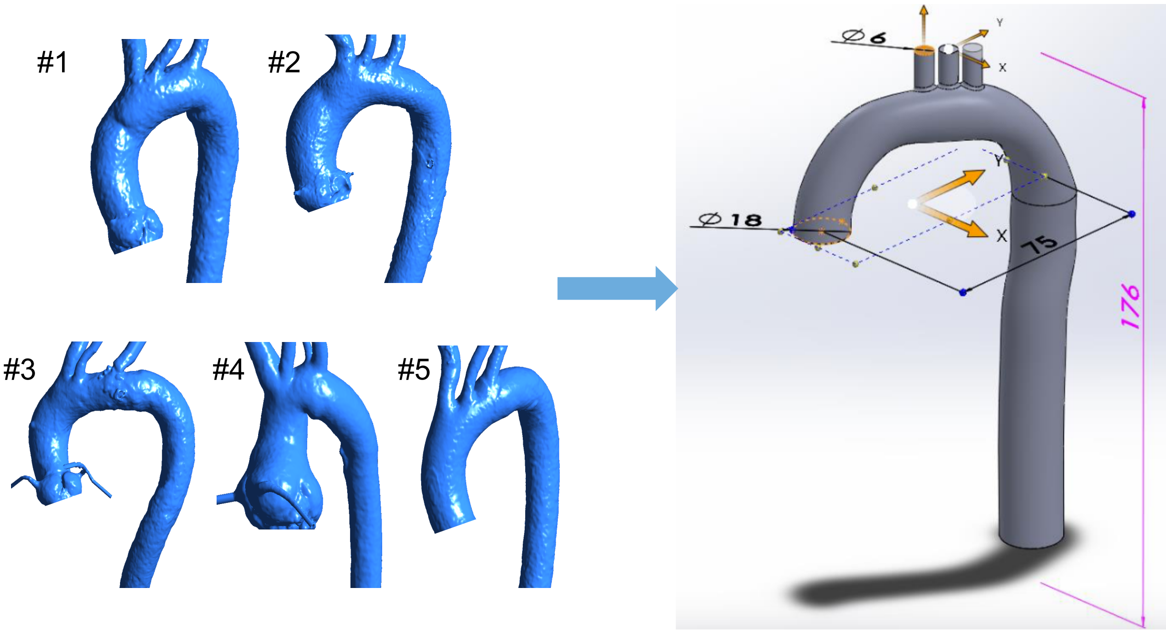

Fig. 1. From patient specific data to a parametric model.

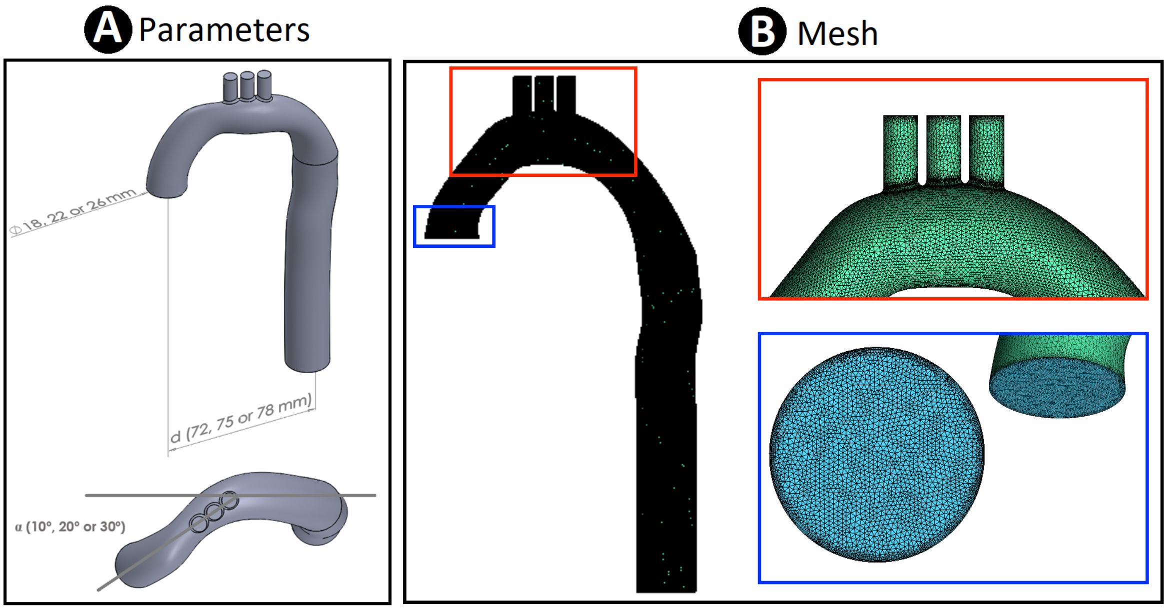

Fig. 2. (A) Definition of the parameters of the idealized aorta geometry. (B) Details of the computational grid.

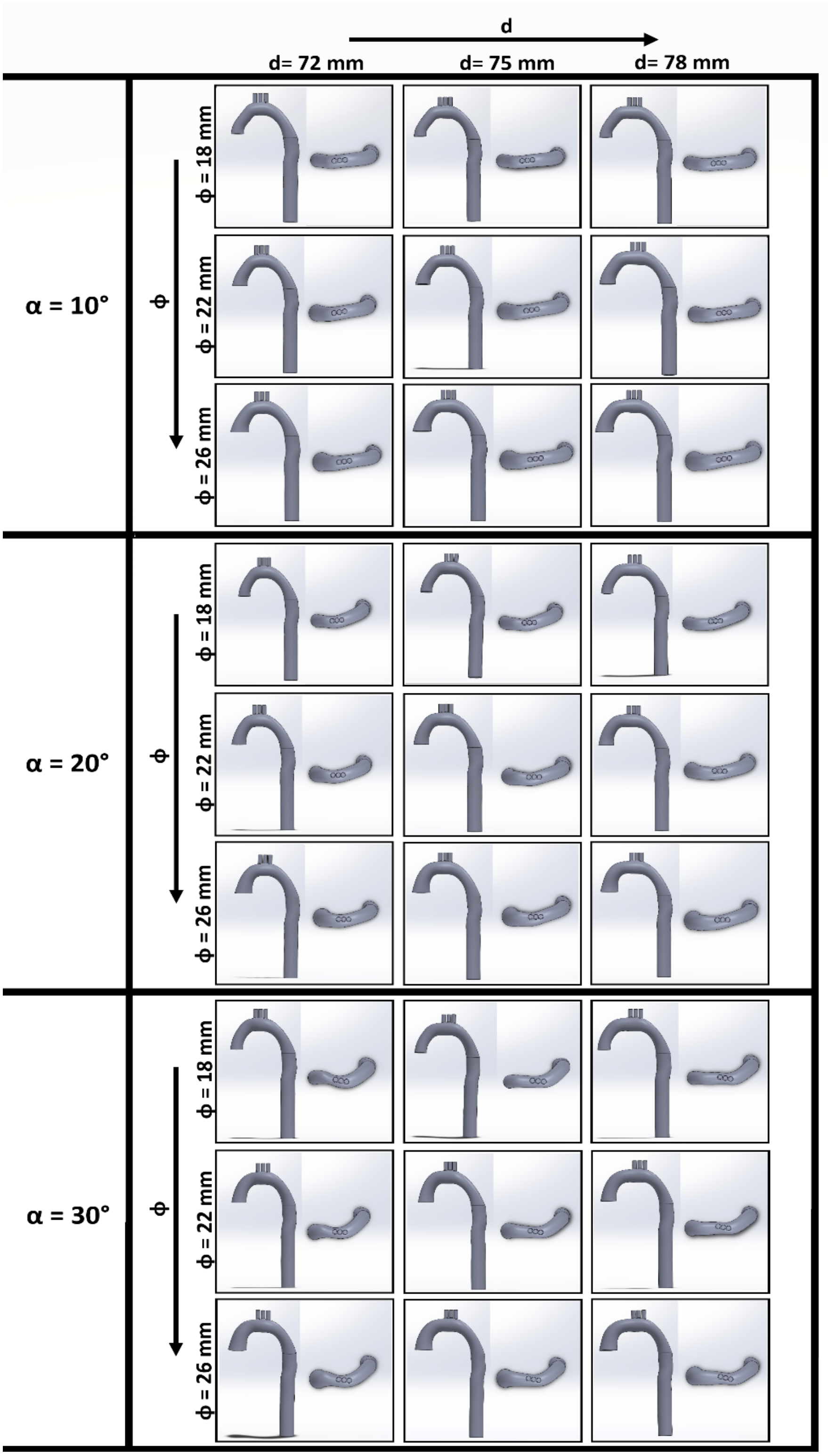

Fig. 3. Overview on the analyzed parameters within the aorta model.

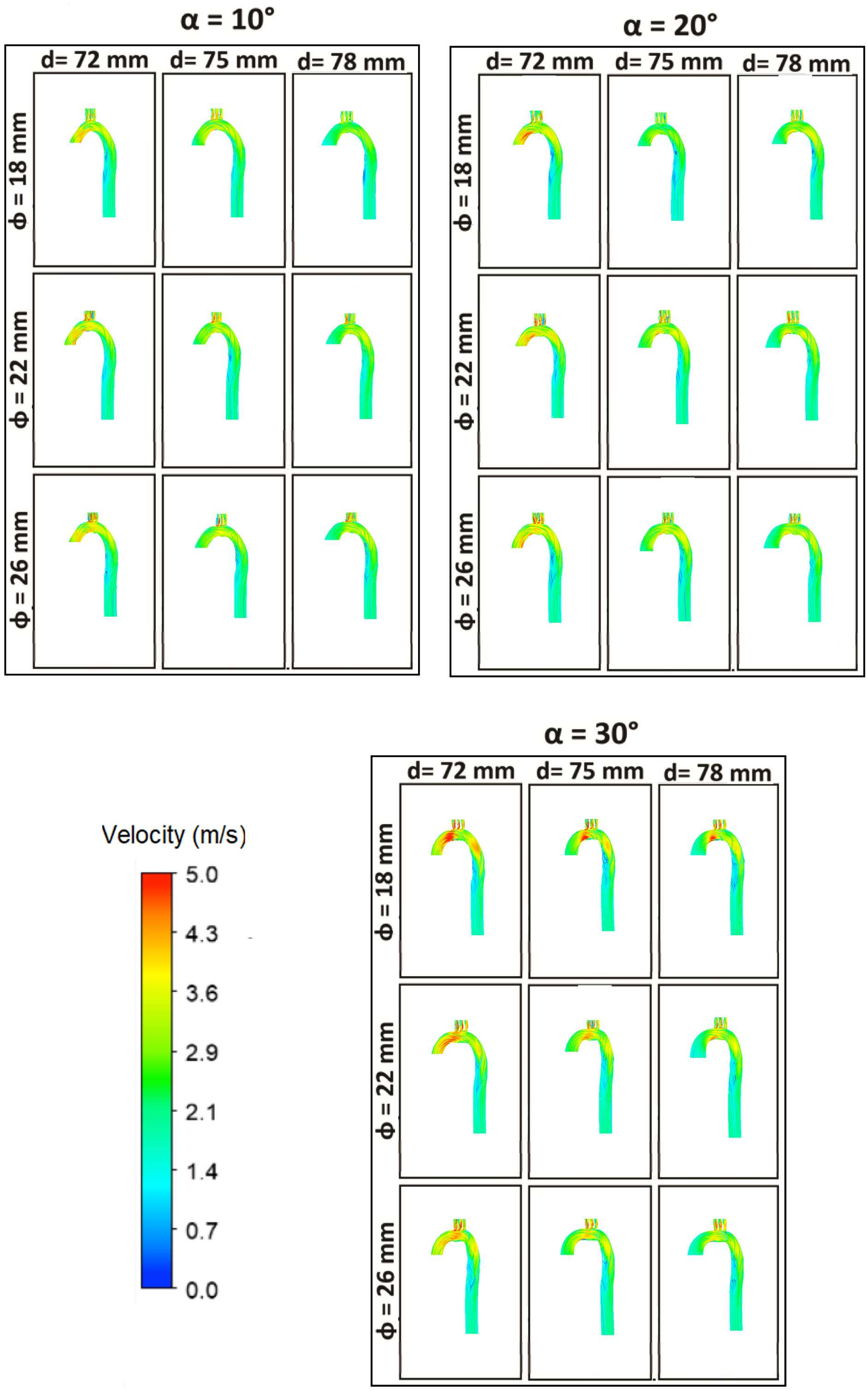

Fig. 4. Flow patterns represented by means of velocity streamlines at peak flow.

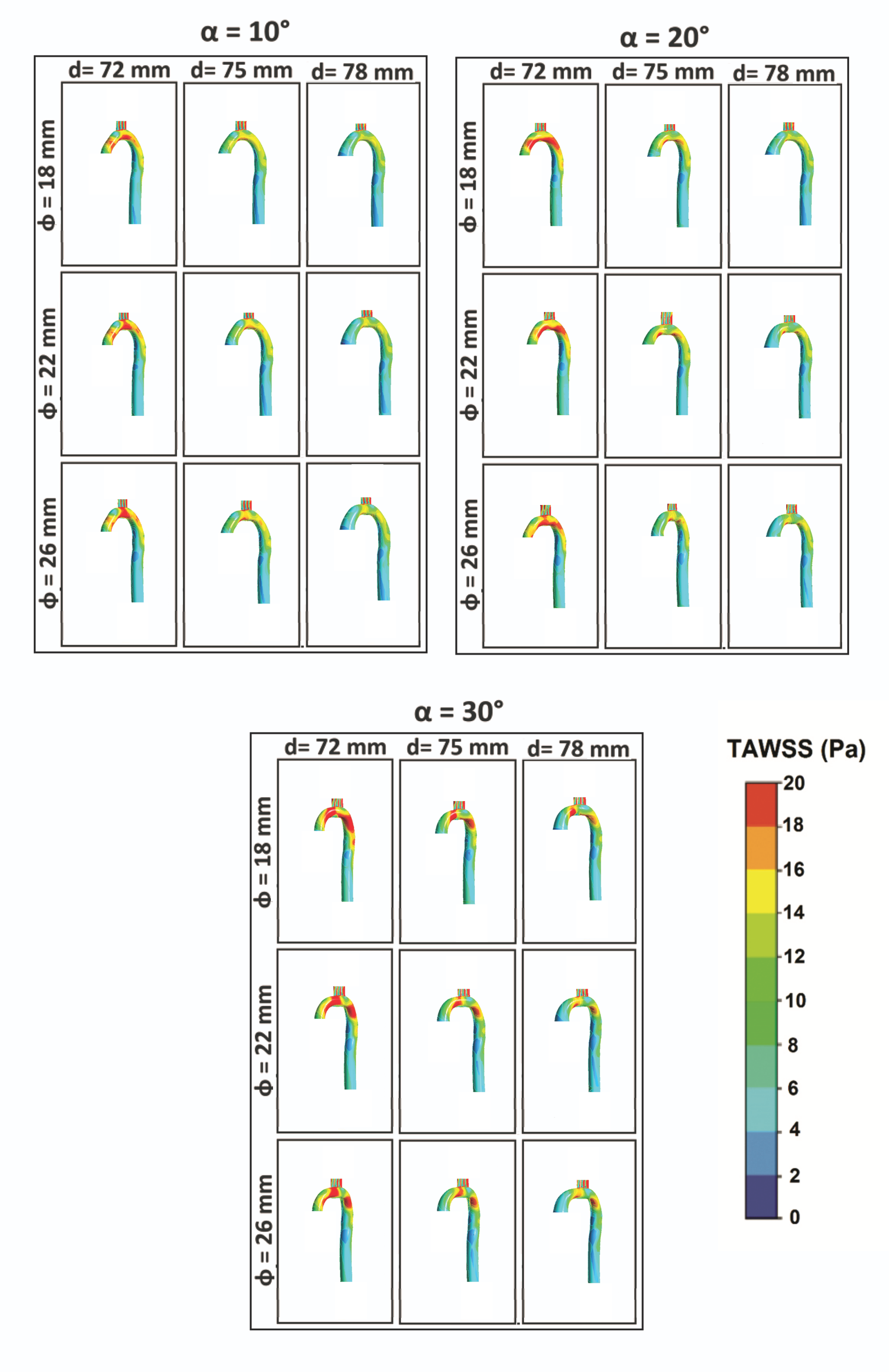

Fig. 5. Spatial distribution of the TAWSS.

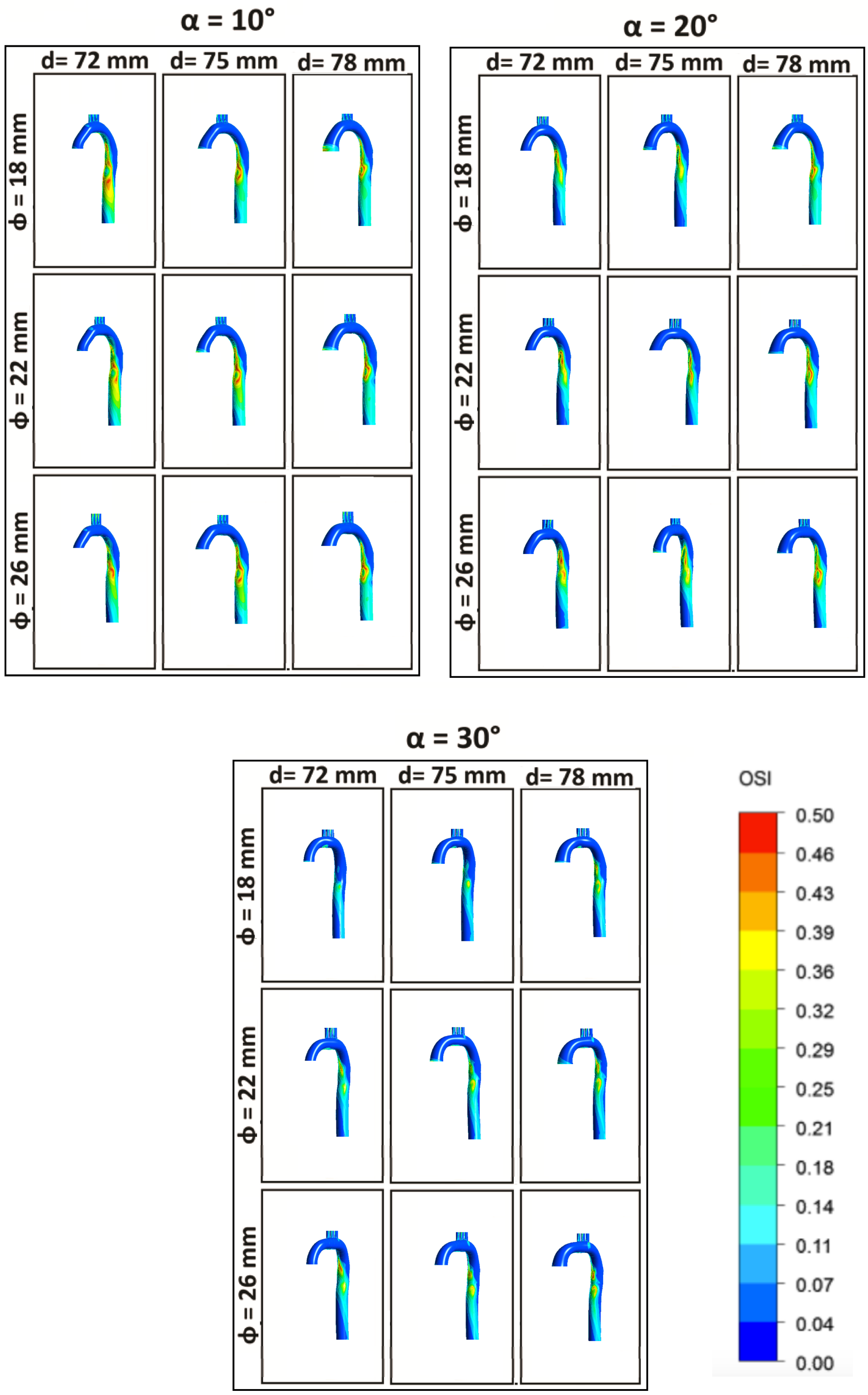

Fig. 6. Spatial distribution of the OSI.

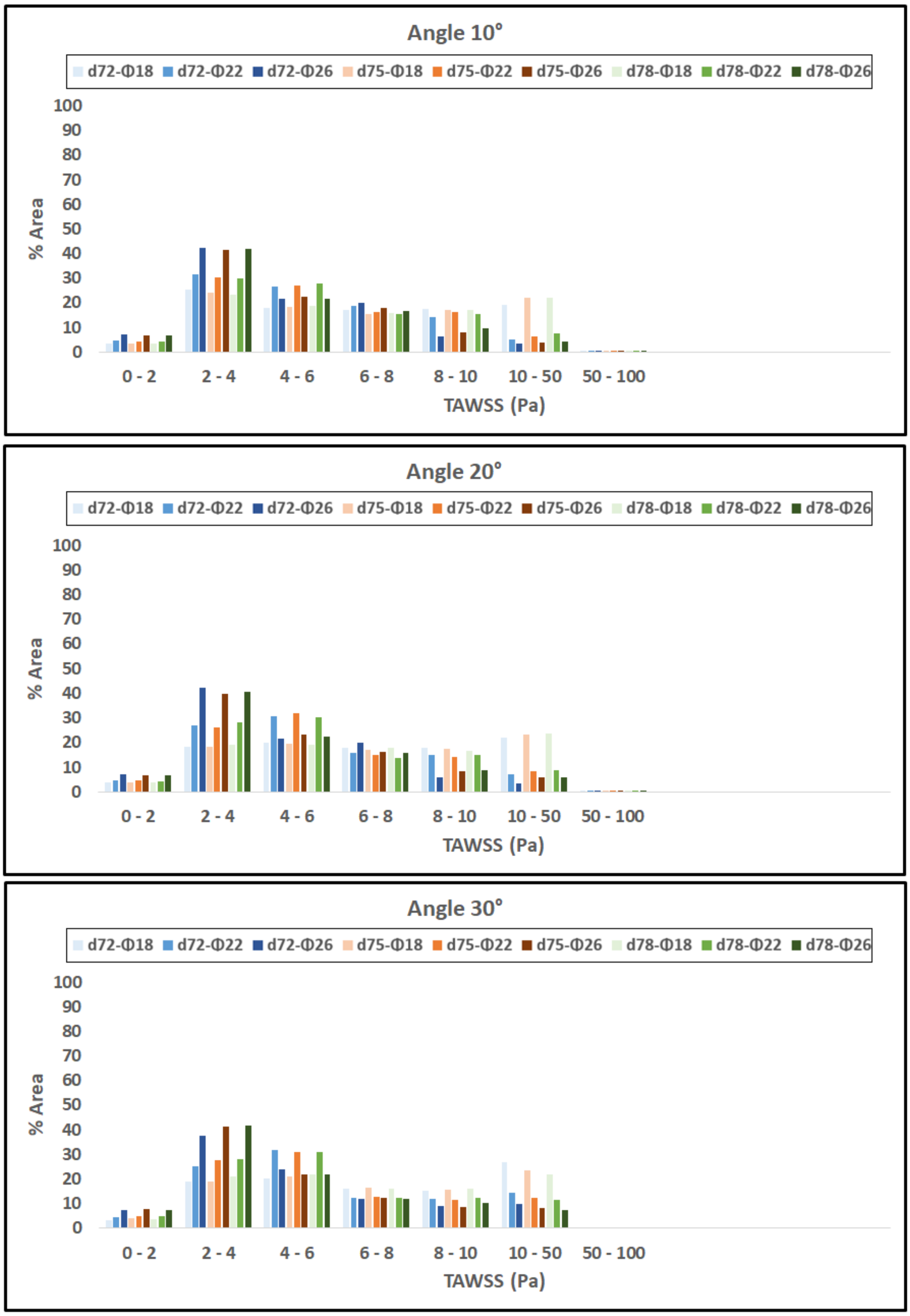

Fig. 7. TAWSS distributions: quantification by means of histograms representing specific intervals of TAWSS as a function of the normalized area of the aorta.

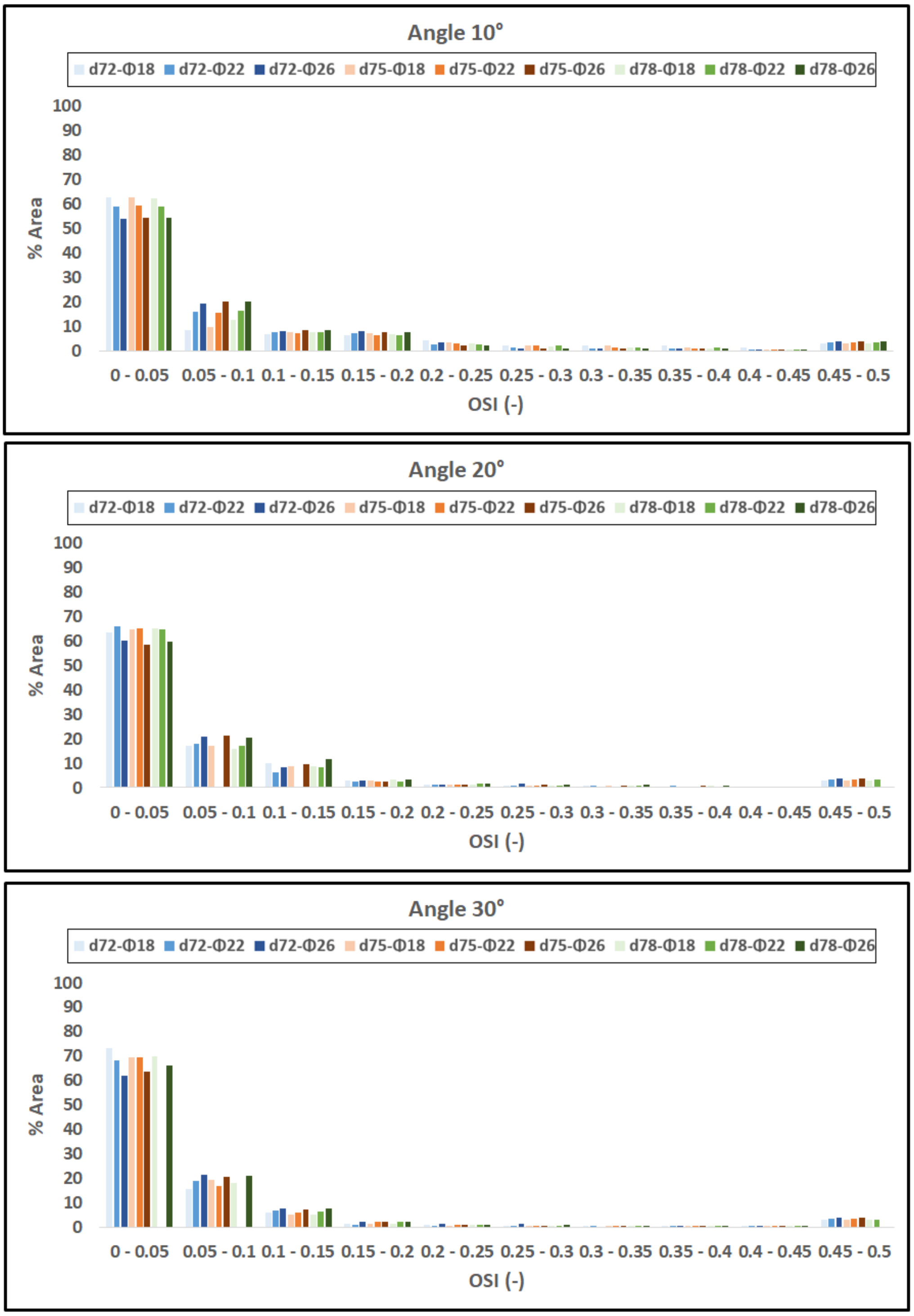

Fig. 8. OSI distributions: quantification by means of histograms that represent specific intervals of OSI as a function of the normalized area of the aorta.

Figure 1

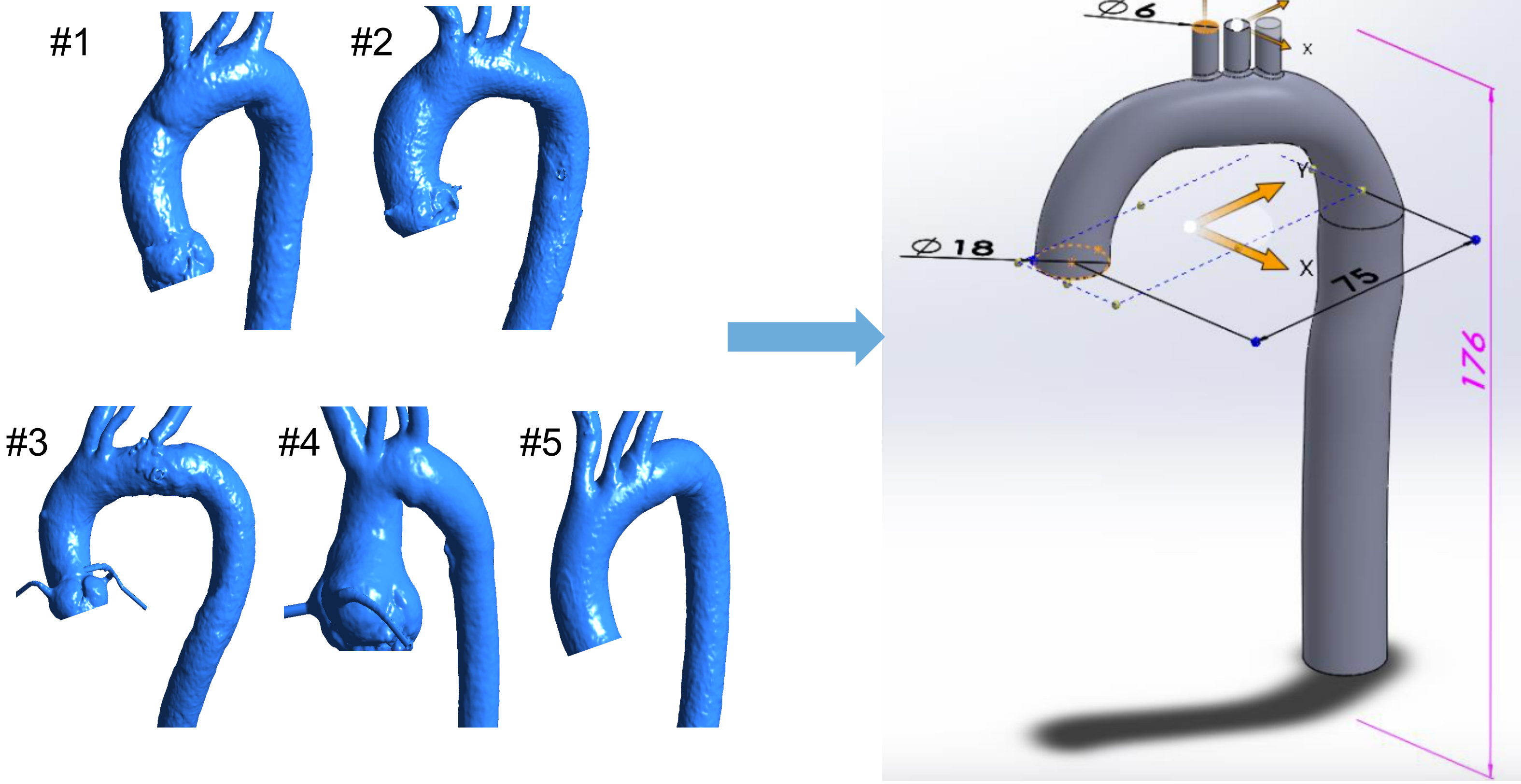

Figure 2

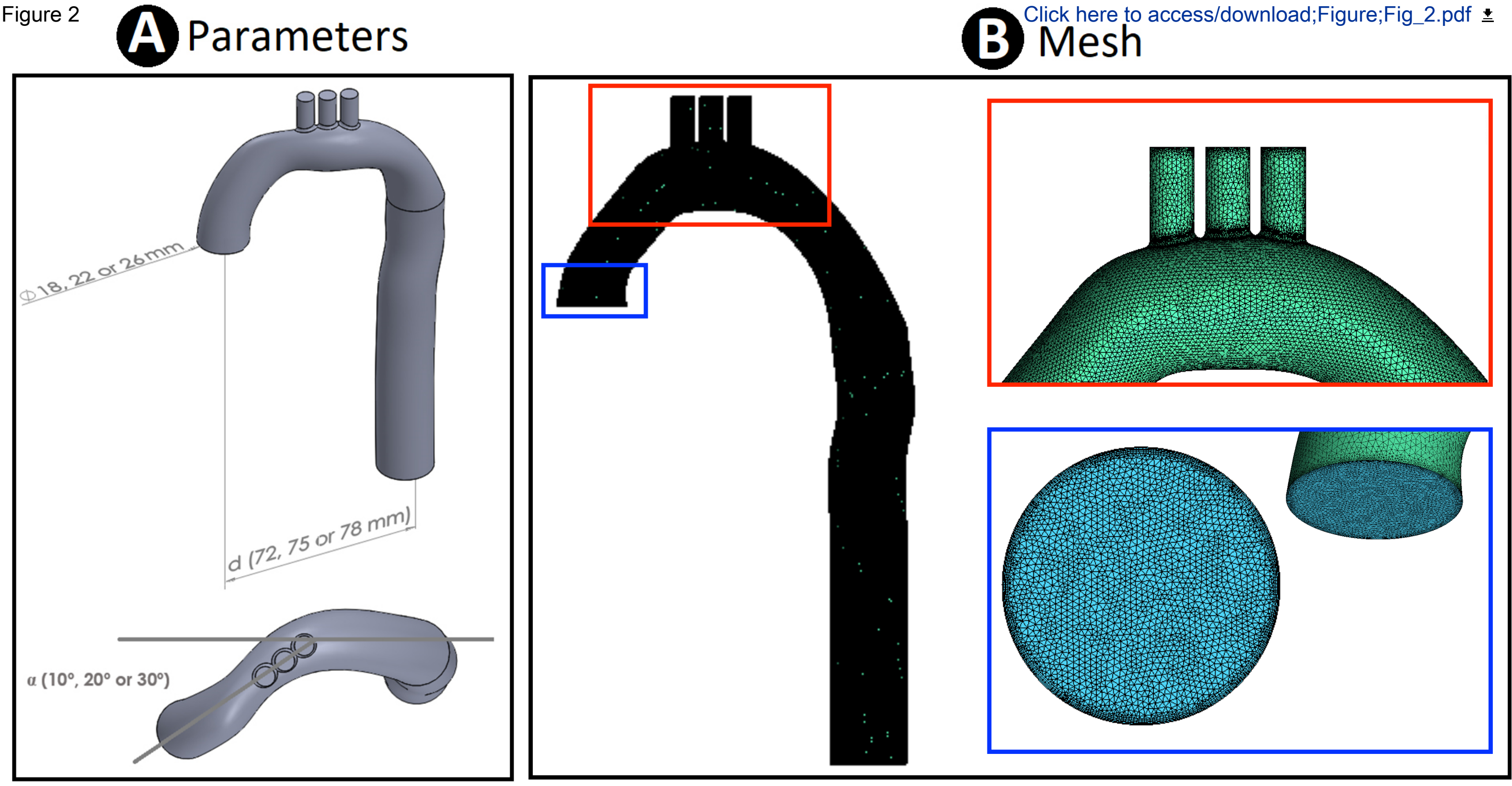

Figure 3

Click here to access/download;Figure;Fig

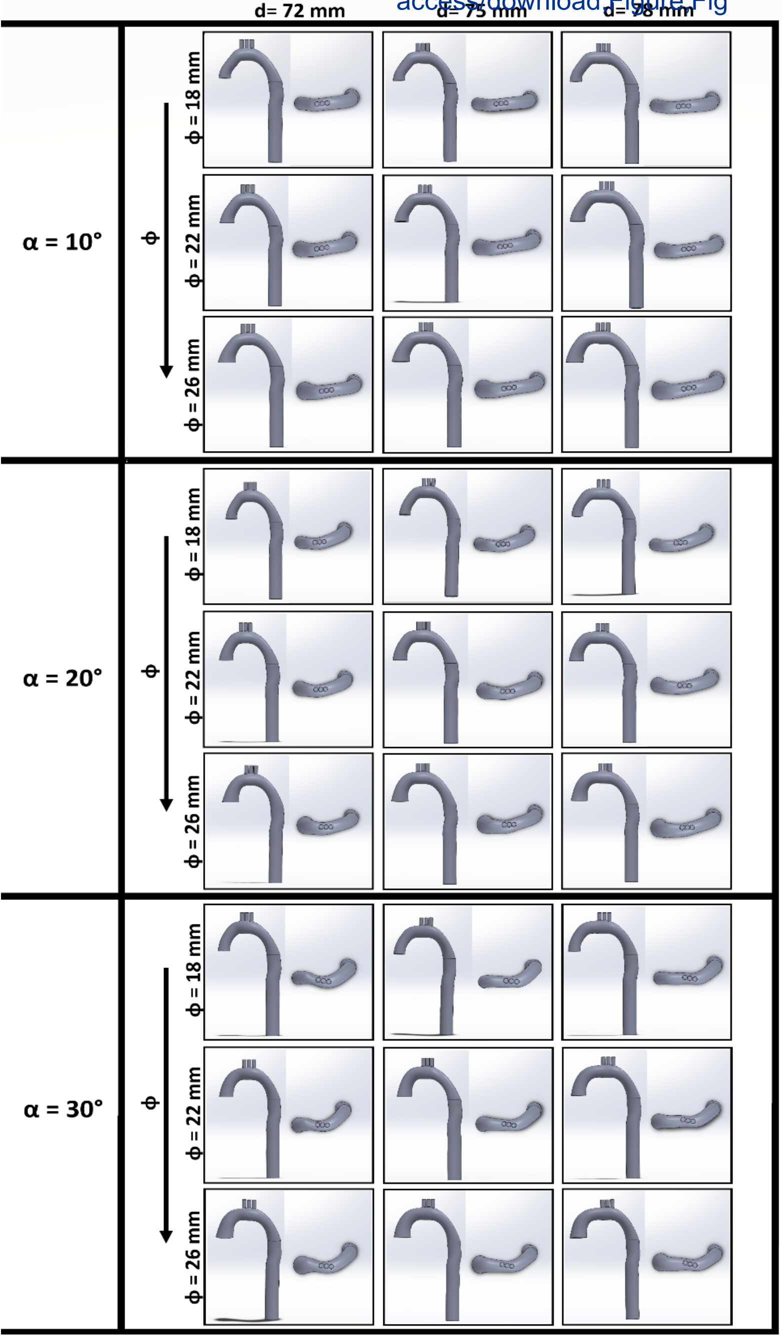

Figure 4

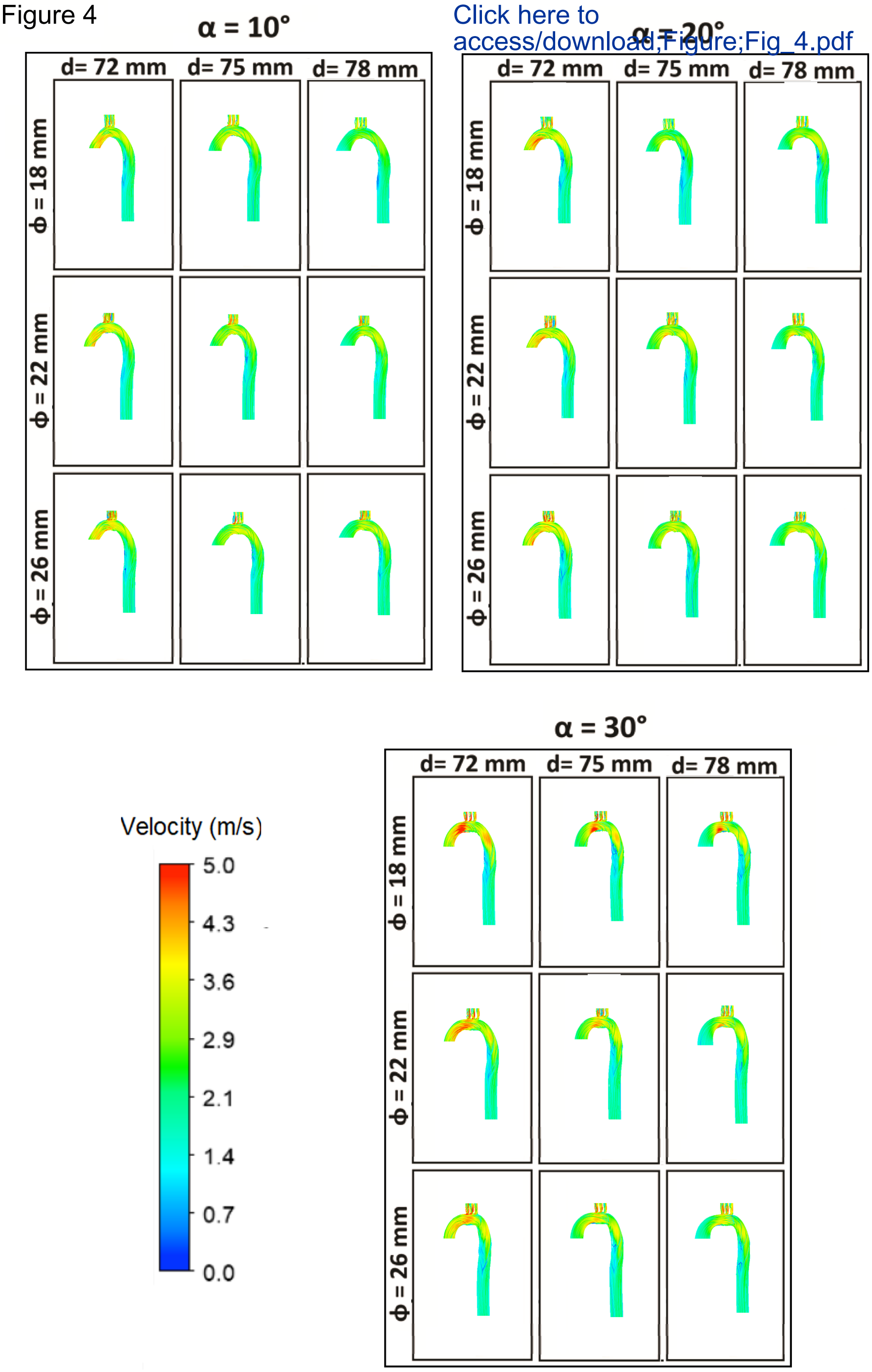

α = 10°
d= 72 mm
d= 75 mm
d= 78 mm
ϕ = 18 mm
ϕ = 22 mm
ϕ = 26 mm
α = 20°
d= 72 mm
d= 75 mm
d= 78 mm
ϕ = 18 mm
ϕ = 22 mm
ϕ = 26 mm
α = 30°
d= 72 mm
d= 75 mm
d= 78 mm
ϕ = 18 mm
ϕ = 22 mm
ϕ = 26 mm
Velocity (m/s)
5.0
4.3
3.6
2.9
2.1
1.4
0.7
0.0

Figure 5

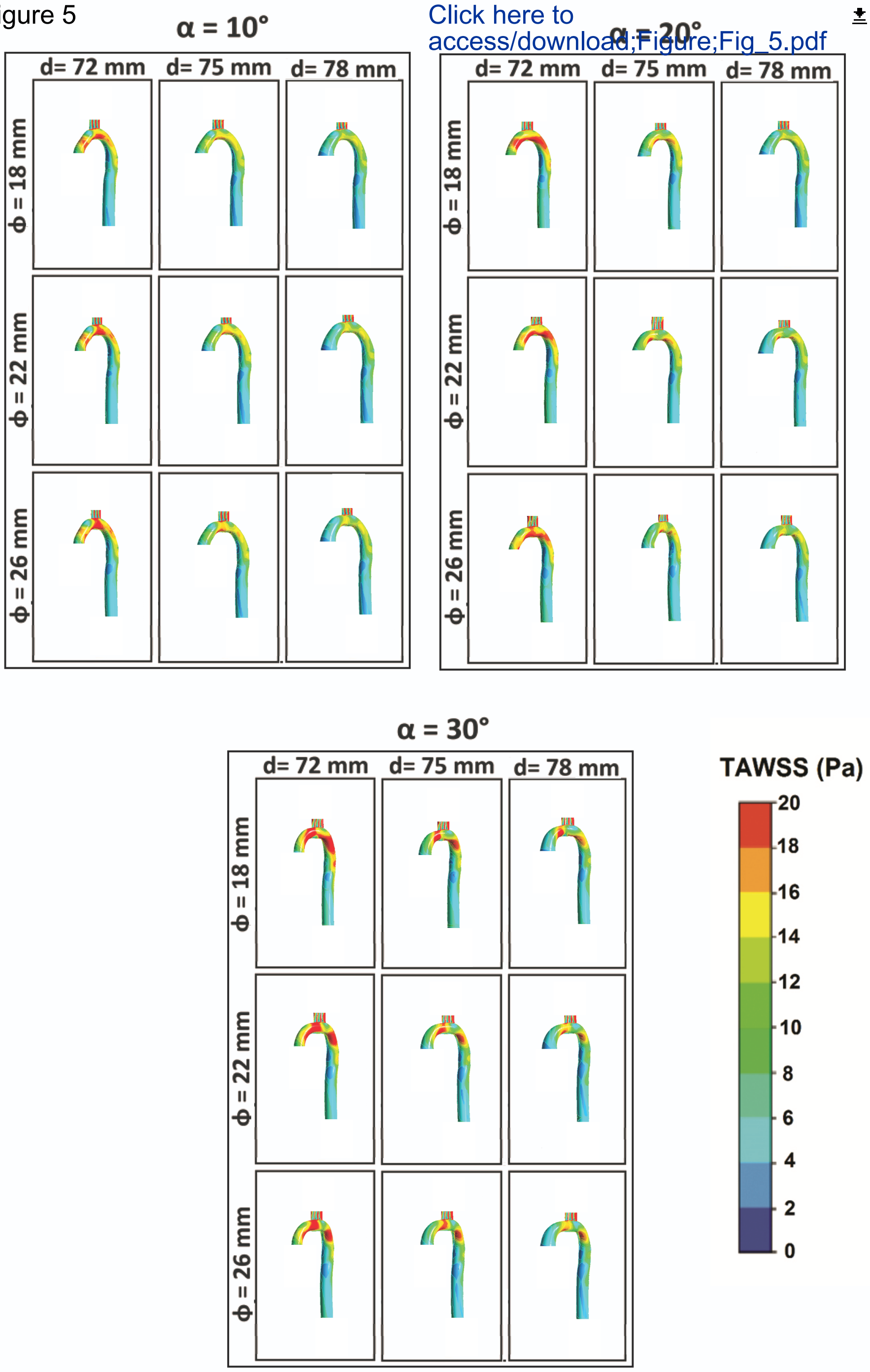
α = 10°
d= 72 mm
d= 75 mm
d= 78 mm
ϕ = 18 mm
ϕ = 22 mm
ϕ = 26 mm
α = 20°
d= 72 mm
d= 75 mm
d= 78 mm
ϕ = 18 mm
ϕ = 22 mm
ϕ = 26 mm
α = 30°
d= 72 mm
d= 75 mm
d= 78 mm
ϕ = 18 mm
ϕ = 22 mm
ϕ = 26 mm
TAWSS (Pa)
20
18
16
14
12
10
8
6
4
2
0

Figure 6

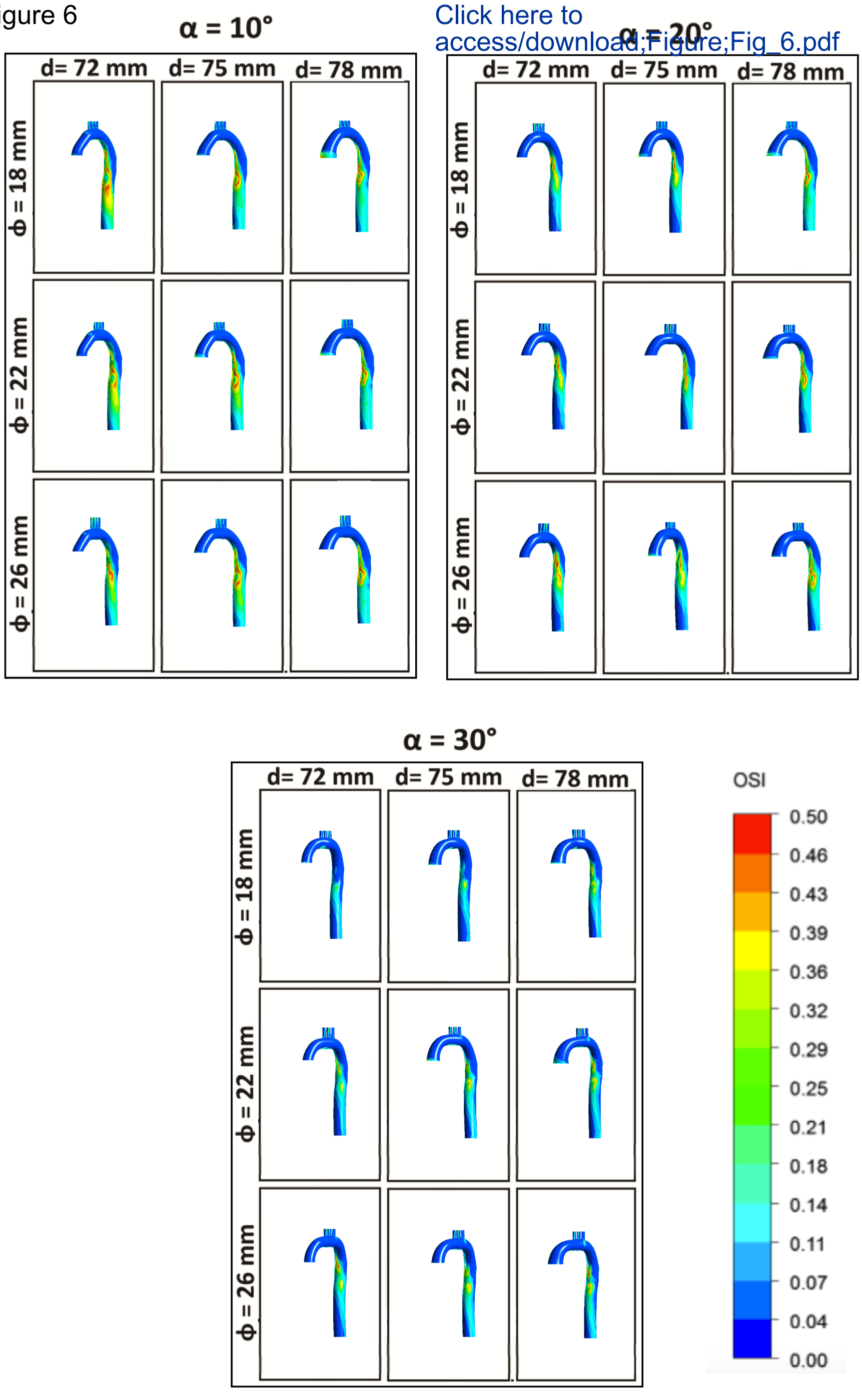
α = 10°
d= 72 mm
d= 75 mm
d= 78 mm
ϕ = 18 mm
ϕ = 22 mm
ϕ = 26 mm
α = 20°
d= 72 mm
d= 75 mm
d= 78 mm
ϕ = 18 mm
ϕ = 22 mm
ϕ = 26 mm
α = 30°
d= 72 mm
d= 75 mm
d= 78 mm
ϕ = 18 mm
ϕ = 22 mm
ϕ = 26 mm
OSI
0.50
0.46
0.43
0.39
0.36
0.32
0.29
0.25
0.21
0.18
0.14
0.11
0.07
0.04
0.00

Figure 7

Click here to access/download;Figure;Fig_7.pdf

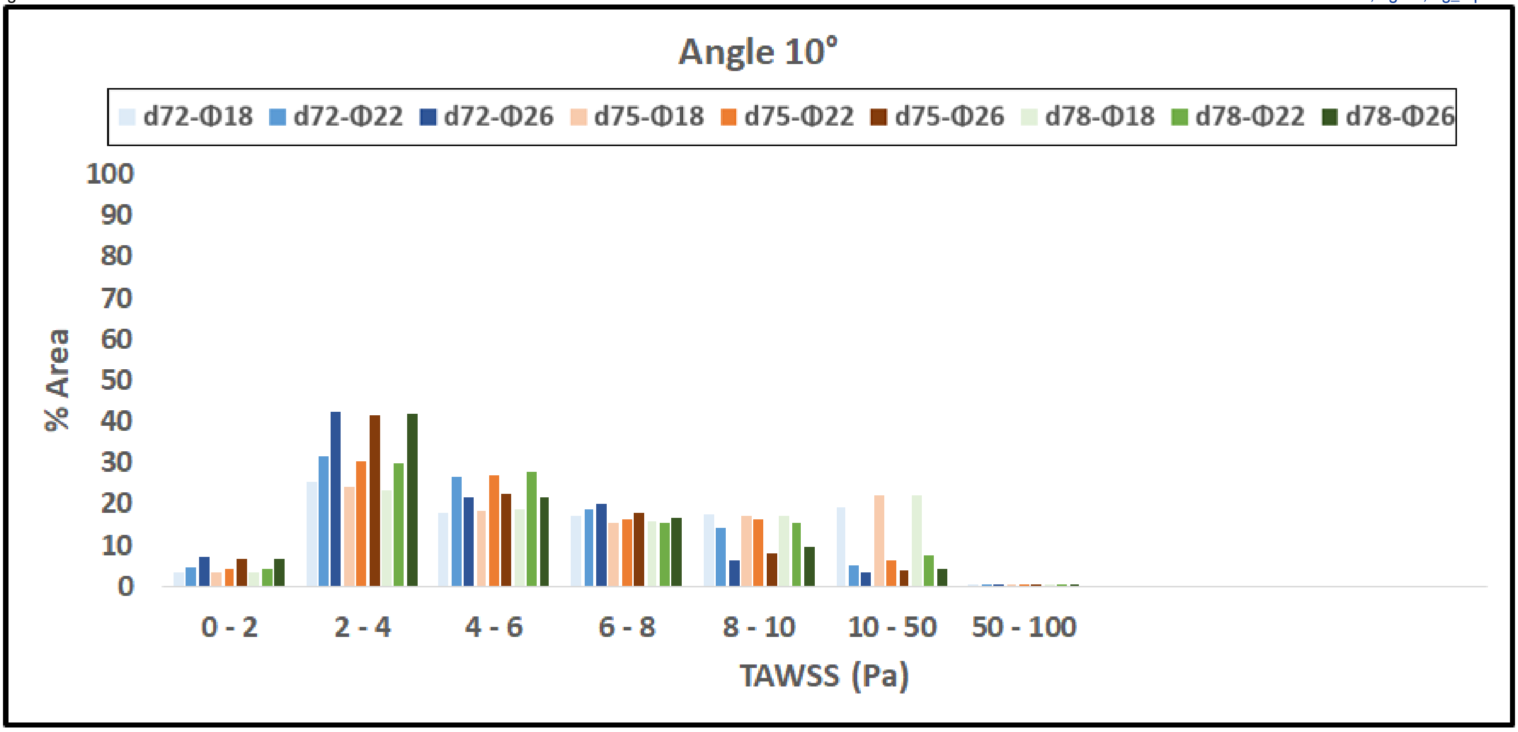

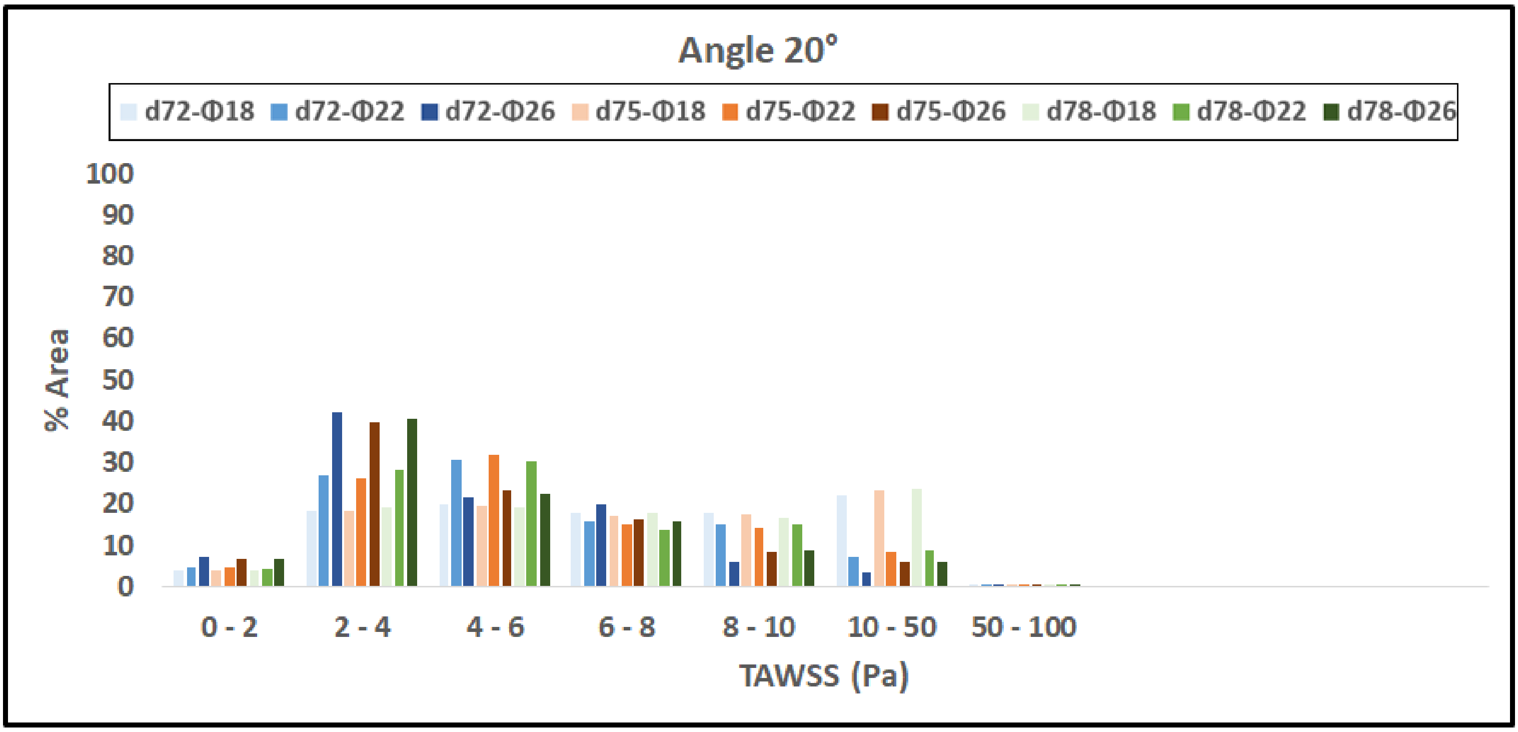

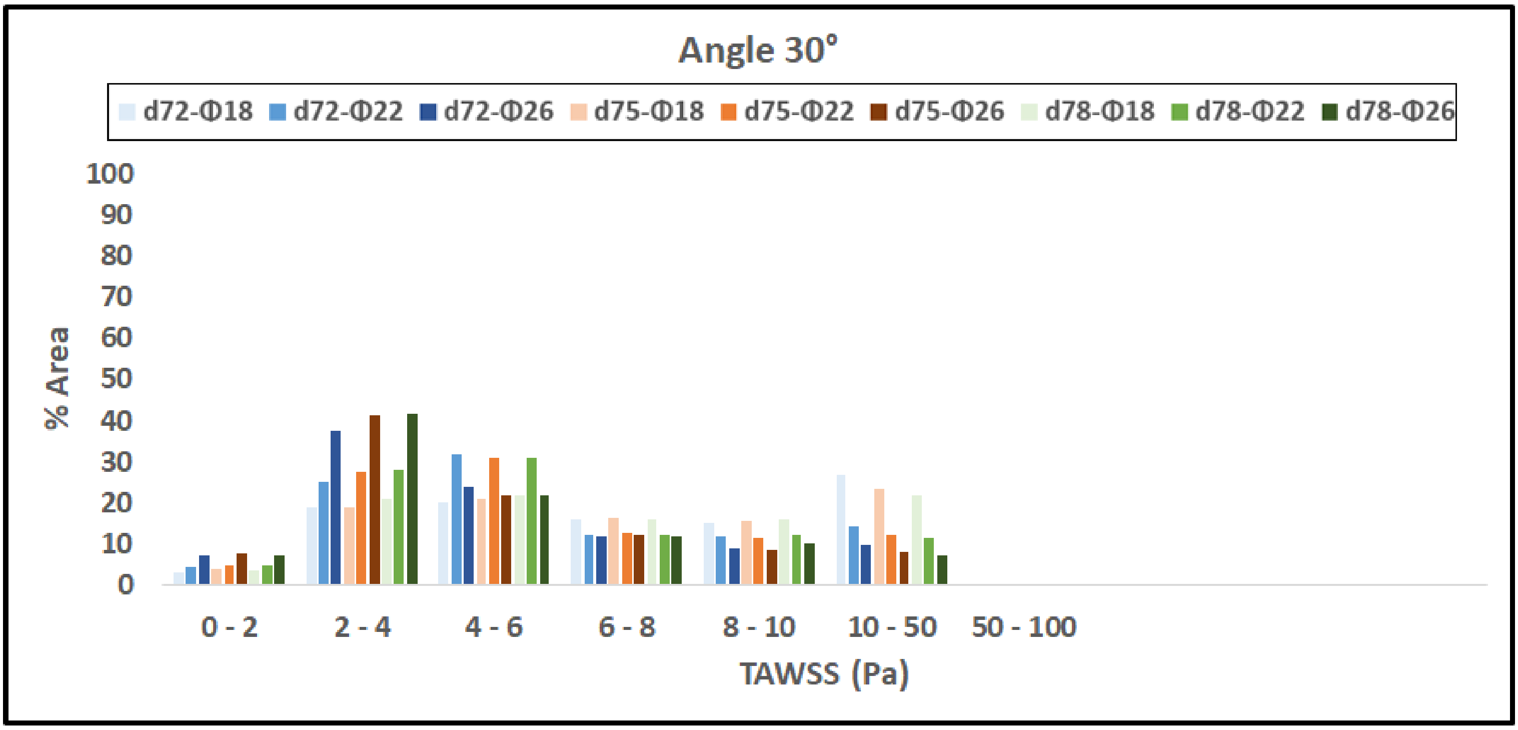

Figure 8

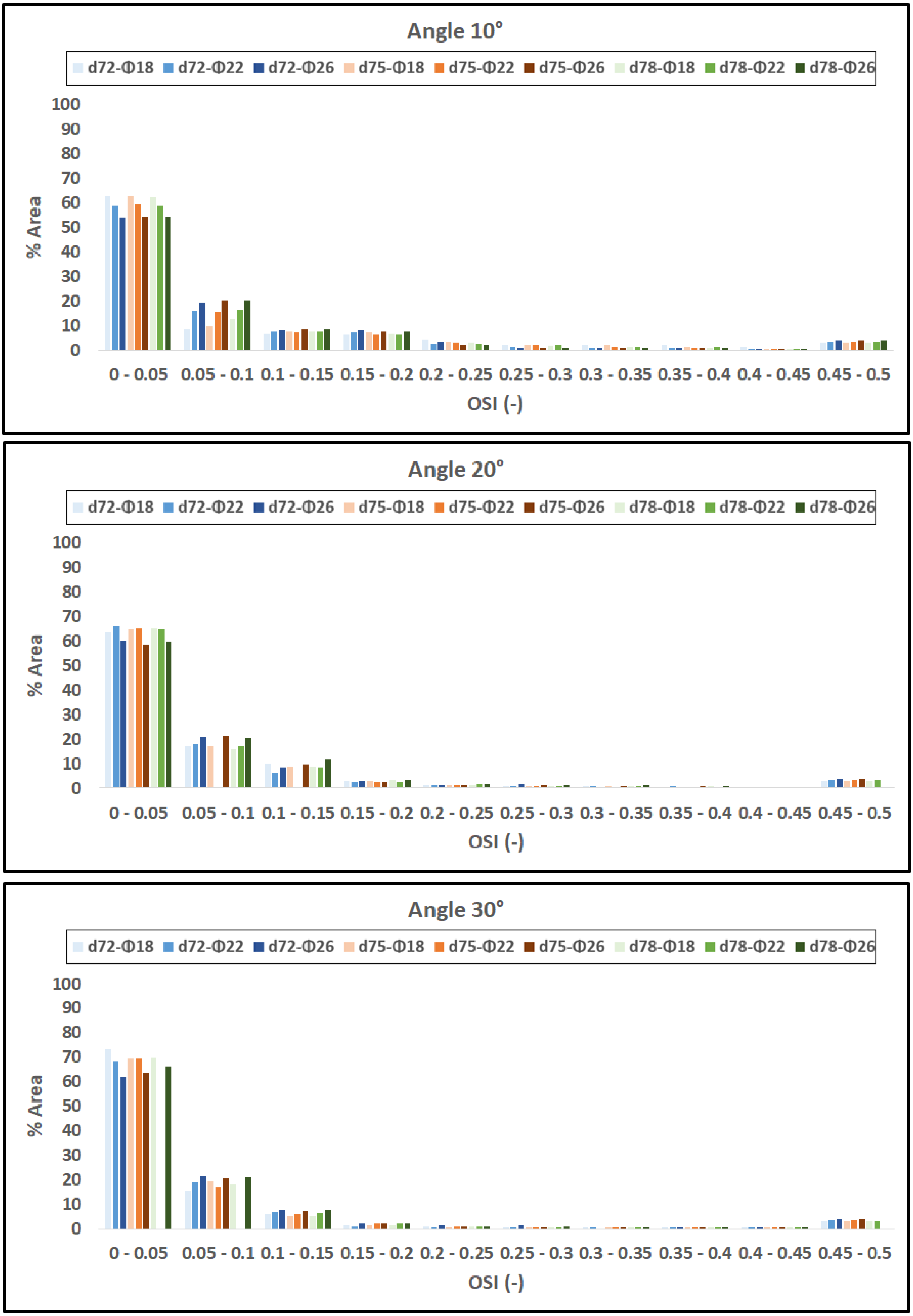
Angle 10°
d72-Φ18 d72-Φ22 d72-Φ26 d75-Φ18 d75-Φ22 d75-Φ26 d78-Φ18 d78-Φ22 d78-Φ26
% Area
0 10 20 30 40 50 60 70 80 90 100
0 - 0.05 0.05 - 0.1 0.1 - 0.15 0.15 - 0.2 0.2 - 0.25 0.25 - 0.3 0.3 - 0.35 0.35 - 0.4 0.4 - 0.45 0.45 - 0.5
OSI (-)
Angle 20°
d72-Φ18 d72-Φ22 d72-Φ26 d75-Φ18 d75-Φ22 d75-Φ26 d78-Φ18 d78-Φ22 d78-Φ26
% Area
0 10 20 30 40 50 60 70 80 90 100
0 - 0.05 0.05 - 0.1 0.1 - 0.15 0.15 - 0.2 0.2 - 0.25 0.25 - 0.3 0.3 - 0.35 0.35 - 0.4 0.4 - 0.45 0.45 - 0.5
OSI (-)
Angle 30°
d72-Φ18 d72-Φ22 d72-Φ26 d75-Φ18 d75-Φ22 d75-Φ26 d78-Φ18 d78-Φ22 d78-Φ26
% Area
0 10 20 30 40 50 60 70 80 90 100
0 - 0.05 0.05 - 0.1 0.1 - 0.15 0.15 - 0.2 0.2 - 0.25 0.25 - 0.3 0.3 - 0.35 0.35 - 0.4 0.4 - 0.45 0.45 - 0.5
OSI (-)

Conflict of interest

None of the authors has any financial or personal relationships that could inappropriately influence (bias) the content of the paper.